

# New Approach to Strong Correlation: Twisting Hubbard into the Orbital Hatsugai-Kohmoto Model

Peizhi Mai<sup>1</sup>, Jinchao Zhao<sup>1</sup>, Gaurav Tenkila<sup>1</sup>, Nico A. Hackner<sup>1</sup>, Dhruv Kush<sup>1</sup>, Derek Pan<sup>1</sup>, Philip W. Phillips<sup>1,†</sup>

<sup>1</sup>*Department of Physics and Institute of Condensed Matter Theory,  
University of Illinois at Urbana-Champaign, Urbana, IL 61801, USA*

(Dated: October 2023)

We present the  $n$ -orbital extension of the Hatsugai-Kohmoto (HK) model to the orbital HK (OHK) model which obtains by covering the Brillouin zone with  $N/n$  Hubbard clusters each containing  $n$ -sites all connected via twisted boundary conditions. We show that this defines a systematic computational scheme to go from  $n = 1$  “band” HK to the full Hubbard model. Further, through powerful scaling arguments, we show that the convergence to Hubbard goes as  $1/n^{2d}$  for  $n^d$ -orbital HK on a  $d$ -dimensional system implying that all the fluctuations vanish in  $d = \infty$ . As evidence for the above, we employ exact diagonalization and DMRG to show that the OHK model matches the exact (from Bethe ansatz) ground state energy of the 1d Hubbard model within 1% with just  $n = 10$  orbitals. For a square lattice, we recover an insulating state regardless of the strength of the interactions, double occupancy in agreement with state of the art simulations, dynamical spectral weight transfer, short-range antiferromagnetic correlations and charge neutral excitations leading to the algebraic temperature dependence of the specific heat, all with a fraction of the computational time of more advanced cluster methods and making it possible to obtain analytical insights. The success of OHK and its rapid convergence to the Hubbard model reiterates that a fixed point controls the physics. Consequently, the  $n$ -orbital HK model offers a new tool for strongly correlated quantum matter.

## INTRODUCTION

The paradigmatic model for strong correlations in quantum matter is that of electrons hopping on a lattice between nearest neighbors but paying the energy cost  $U$  anytime they doubly occupy the same site. Naively, the energy eigenstates of this model would seem to be ordered with respect to the number of doubly occupied sites. However, this fails because the potential and kinetic terms do not commute. As a result, electrons can lower their energy by hopping to sites with single occupancy. It is for this reason that this simple model remains unsolved in any dimension exceeding unity, thereby remaining a grand challenge as it is the gold standard for Mott physics in the cuprates. The state-of-the-art remains quantum Monte Carlo[1–5], density matrix renormalization group (DMRG)[1–3, 6] and dynamical mean-field theory (DMFT)[7–9] and its cluster versions such as cellular DMFT[10, 11] and the dynamical cluster approximation (DCA)[12–15] which have all been useful in unveiling the properties of the Hubbard model including the pseudogap[12, 16–19], superconductivity[3, 12] and transport[9, 20, 21] in the strange metal regime.

A natural question arises: Is there an alternative? The more tractable formulation of Mott physics is the Hatsugai-Kohmoto (HK) model[22] which we refer to as the band HK model in the following. It has a repulsion between any two electrons with opposite spin that doubly occupy the same momentum state. Consequently, the doubly occupied band steadily increases in energy as the repulsion increases resulting in an insulating state in a half-filled band when the interaction strength exceeds the bandwidth. In this model, double occupancy is the organizing principle for the ordering of the eigenstates. Clearly then, this is a gross simplification of the Hubbard model stemming from the locality in momentum space (long-range interactions in real space) and generating

a macroscopic spin degeneracy in the singly occupied sector. In essence, the solvability of band HK rests on the commutativity of the potential and kinetic energy terms. Can such non-commutativity be put back in systematically, thereby reducing the difference with the Hubbard model, without giving up on exact solvability?

We show here that this can be done. Our work shows that two rather seemingly disparate approaches, the momentum-space or band HK model and the exact diagonalization (ED) of small Hubbard clusters share a fundamental link. Our work here is based on an orbital extension of the HK model in which each  $k$ -state is decorated by  $n$  local (orbital) degrees of freedom. To show the power of the model, we present at the outset Fig. 1(a) which compares the exact Bethe ansatz results in one dimension (1d) for the ground state energy with the orbital HK (OHK) model as a function of the number of orbitals,  $n$ . As  $n$  increases, the OHK model rapidly approaches the exact result. Already at  $n = 10$ , the deviation from the exact result is less than 1%. Precisely why this agreement with the Hubbard model is expected as  $n$  increases is the subject of this paper. What we establish here is that as  $n \rightarrow N_{\text{sites}}$ , the OHK model is exactly the Hubbard model regardless of the spatial dimension. Where possible, we compare with existing methodology. In particular, we show that with a few orbitals, the OHK model recovers all known results in 1d is even more convergent than the standard tool in 1d (density matrix renormalization group (DMRG)) and is in agreement with standard results in two dimensions (2d) for the Mott transition[7, 12], and spin susceptibility[23], spectral function[24, 25], double occupancy[23, 26], dynamical spectral weight transfer[27, 28], and heat capacity[29, 30]. The nature of the rapid convergence is explained in the scaling argument in the penultimate section. In essence, the orbital HK model is an efficient and cost-effective simulator of Mott/Hubbard physics, enabling analytical insights and numerical augmentation. This is a consequence of the flow

of OHK to the Mott fixed point in which a discrete  $Z_2$  symmetry is broken[31].

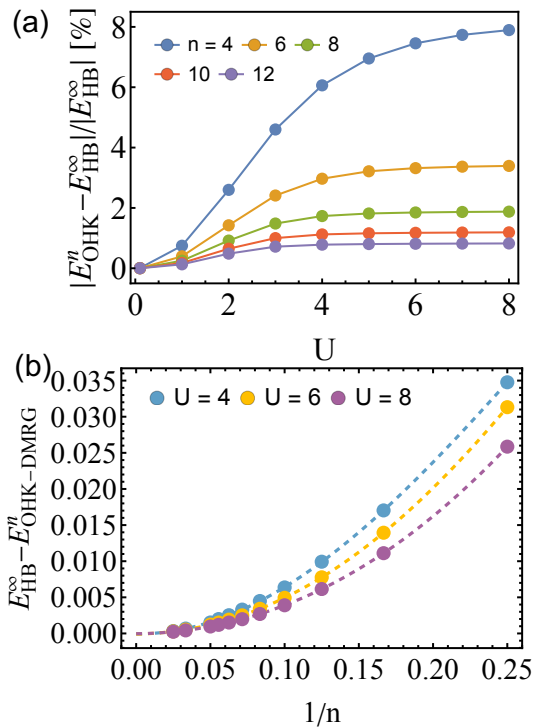


FIG. 1: Comparison of the difference between the ground-state energy with  $n$ -OHK model,  $E_{\text{HK}}^n$ , and the infinite-system size Hubbard Bethe ansatz energy,  $E_{\text{HB}}^{\infty}$ . (a) OHK is solved by ED. (b) OHK (blue dots) is solved by DMRG including as many as 40 orbitals at  $U = 4$ . The dashed line is a machine learning polynomial regression fitting with extrapolation to  $1/n \rightarrow 0$  ( $n \rightarrow \infty$ ). The asymptotic values at  $1/n = 0$  are  $-5.4 \times 10^{-5}$  ( $U = 4$ ),  $-9 \times 10^{-5}$  ( $U = 6$ ),  $-4 \times 10^{-5}$  ( $U = 8$ ). The fitting curves can be well represented as  $f(U = 4) = 0.45(1/n^{1.83})$ ,  $f(U = 6) = 0.51(1/n^{2.01})$  and  $f(U = 8) = 0.45(1/n^{2.07})$ .

## LOCAL CORRELATIONS

The starting point for our analysis is Fig. 2a which shows that although the HK model has all-to-all interactions, the hole 2-point correlator,  $g_h(r)$ , (blue dots) is identical to that of the non-interacting correlator (orange squares) for a metallic density of  $n = 0.75$ . To compensate for bifurcation of the spectral weight in the HK case, we set the density of the non-interacting system to  $2 \times 0.75 = 1.5$  and multiplied the corresponding  $g_h(r)$  by  $1/2$ . See Supplemental Material (Figs. S5 and S6) for further details on the evolution of exponential decay at half-filled insulator to the algebraic fall-off in the doped metallic system. The fact that the two are coincident implies that the interacting HK and non-interacting Fermi liquid are equally local. The same is true for the 4-point and all higher correlation functions. This is significant because Wightman's reconstruction theorem[32] ensures that if all the

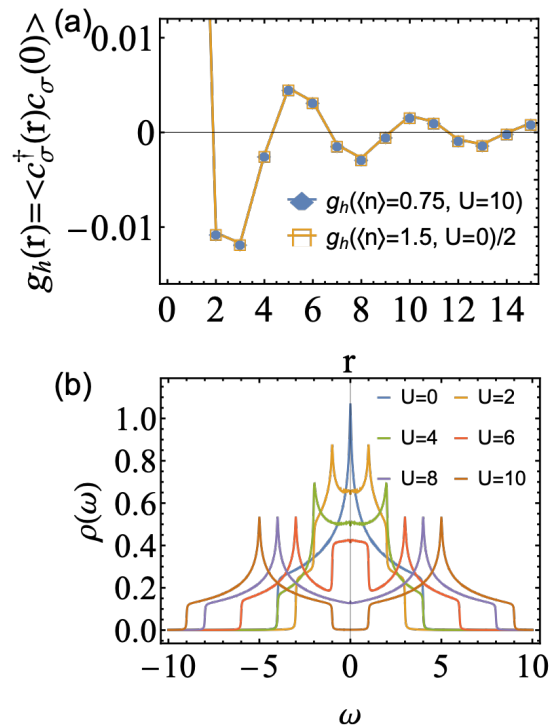


FIG. 2: (a) 2-point correlator showing the absence of long-range correlations in the 2d band HK model at different densities despite the all-to-all nature of the interactions in real space with  $U/t = 10$  and  $\beta = 50/t$ . Here  $r = r_x = r_y$ . (b) The density of states under different  $U$  displaying Mott transition at the half-filled band HK model with  $\beta = 200/t$ .

$n$ -point functions are local, then so is the theory. The question arises, why does a model admit non-local interactions at the level of the Hamiltonian but exhibit purely local real-space correlations? To gain insight into this, we plot in Fig. 2b the density of states for various  $U$  across the Mott transition of the half-filled band HK model, which interestingly has never been computed. Here the Mott transition to the insulating state proceeds via depletion of the density of states at the central peak at  $\omega = 0$ , similar to that in the standard single-site DMFT simulation[7]. This is telling and consistent with the locality of the  $n$ -point correlators. Ultimately, the Hamiltonian of the band HK model can be mapped onto a local model. In fact, it is identical in form to the atomic limit[33] of the Hubbard model with the band index  $\mathbf{k}$  replacing the site index  $\mathbf{i}$ . A more precise statement will be made later when we complete the mapping to the full Hubbard model. In fact, we present in the conclusion a scaling argument showing how precisely the  $d = \infty$  limit obtains.

## ORBITAL HK

Given that the band HK model is ultimately local, it should be generalizable to include the non-commutativity of the ki-

netic and potential energies. As pointed out previously[33], band HK can be generalized to include multiple orbitals per  $\mathbf{k}$ -state as is necessary for the adaption of this model to topological models, all of which have at least 2 atoms per unit cell[34, 35]. Such a change produces qualitatively new physics as the hybridization between the orbitals lifts[33] the thermodynamic degeneracy of the band HK model while preserving only the degeneracy constraint by the symmetry[36]. Inspired by that, we adopt an OHK model to capture the strongly correlated dynamical mixing in a simple square lattice by redefining a set of lattice sites as orbitals. This leads to a reduction in the size of the Brillouin zone (BZ) scaling as  $1/n$ , referred to as the reduced Brillouin zone (rBZ $_n$ ), as it depends on the orbital number  $n$  and shown in Fig. 3. As we will see, the convergence of this model to the exact result is faster than this, roughly scaling as  $1/n^2$ .

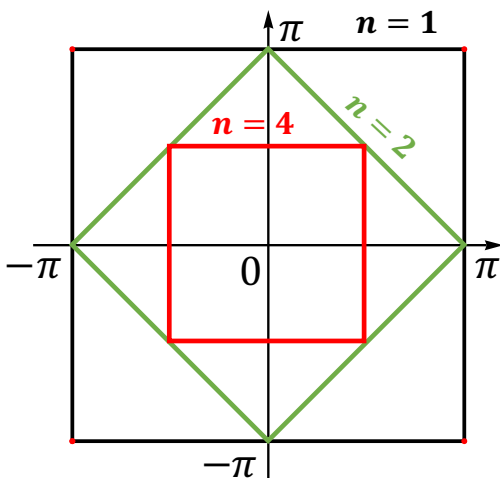


FIG. 3: Evolution of the reduced Brillouin zone (with the constraint  $N \times n = N_{\text{sites}}$ ) as the number of orbitals ( $n$ ) increases, leading to a purely local (in  $\mathbf{k}$ -space) model when  $n = N_{\text{sites}}$ .

The most general version of this model is given by

$$H_{\text{OHK}} = \sum_{\mathbf{k}, \alpha, \alpha', \sigma} g_{\alpha, \alpha'}(\mathbf{k}) c_{\mathbf{k}\alpha\sigma}^\dagger c_{\mathbf{k}\alpha'\sigma} - \mu \sum_{\mathbf{k}, \alpha} n_{\mathbf{k}\alpha, \sigma} + \sum_{\mathbf{k}, \alpha, \alpha'} U_{\alpha, \alpha'} n_{\mathbf{k}\alpha\uparrow} n_{\mathbf{k}\alpha'\downarrow}, \quad (1)$$

where  $k$  is summed over the rBZ $_n$  and  $g(\mathbf{k})$  is the dispersion matrix, determined by the underlying lattice hopping process and orbital setup,  $\alpha(\alpha')$  is the orbital index (ranging 1 to  $n$ ) and  $\sigma$  is the spin. Note while the kinetic and potential energies no longer commute, the Hamiltonian still maintains the form  $\sum_k h_k$  and hence is still exactly solvable and thus governed by the HK fixed point[31, 37]. Fig. 3 depicts the reduction of the Brillouin zone when  $n$  orbitals decorate each  $\mathbf{k}$ -point (see supplemental Fig. S7 for real-space counterparts). As a reduction of the Brillouin zone, in the limit of  $n \rightarrow N_{\text{sites}}$ , the  $\mathbf{k}$ -summation vanishes reducing the interaction term entirely

to,

$$\lim_{n \rightarrow N_{\text{sites}}} \sum_{\alpha, \alpha'=1}^n \sum_{\mathbf{k} \in \text{rBZ}_n} U_{\alpha, \alpha'} n_{\mathbf{k}\alpha\uparrow} n_{\mathbf{k}\alpha'\downarrow} = \sum_{\alpha, \alpha'=1}^{N_{\text{sites}}} U_{\alpha, \alpha'} n_{\alpha\uparrow} n_{\alpha'\downarrow}, \quad (2)$$

which is just a summation over the local degrees of freedom as in the generalized Hubbard model. The on-site Hubbard model results by just contracting the  $\alpha$  and  $\alpha'$  indices. Hence, we are guaranteed to obtain Hubbard physics for  $n$  sufficiently large. Rather than the  $1/n$  convergence, the real convergence as computed from the difference between the computed OHK ground state energy and the exact Bethe ansatz result, scales as  $1/n^\gamma$  with  $\gamma > 1$  ( $\gamma = 1.83$  for  $U = 4$  and increases for larger  $U$  reaching  $\gamma = 2.07$  for  $U = 8$  as shown in Fig. 1(b)). To construct Fig. 1(b), we used DMRG to solve OHK with  $n$  as large as 40. Such an orbital number exceeds the limitations of ED (Supplemental Figs. S2 and S3 contain the full data sets). Hence, the calculations in Fig. 1(b) directly parallel the Hubbard-DMRG study in Fig. 3 in the supplement which shows a  $1/L$ ,  $L$  the chain length, convergence as is expected for a purely variational technique. In direct contrast lies the OHK convergence of  $1/n^2$ , significantly faster than the  $1/L$  in DMRG. Our ability to solve OHK at least in 1d by DMRG reinforces that we are not limited to compute the energy in OHK with ED. To reinforce the simplicity of the method, all calculations were performed on a personal computer. This example demonstrates that OHK can combine with state-of-the-art numerical methods as well as data-driven techniques to predict the  $n \rightarrow N_{\text{sites}}$  limit with a convergence (see Fig. S3) that exceeds even the gold-standard, DMRG. More examples can be found in supplemental Fig. S3. We also compare (supplemental Fig. S4) the charge gap,  $\Delta$ , in both OHK-ED and Hubbard-DMRG.  $\Delta$  vanishes in OHK (as it is in the thermodynamic limit) when  $U \rightarrow 0$  whereas it is finite in Hubbard-DMRG as limited by the finite system size.

Since we have established the convergence could be as rapid as  $1/n^2$ , we apply the OHK to 2d because unlike Hubbard-DMRG, the OHK model is easily extendable to higher dimensions. All that is necessary is to arrange the  $n$  orbitals in a cluster having the symmetry of the underlying lattice. For  $n = 4$ , implemented here as a  $2 \times 2$  cluster, the matrix  $g(\mathbf{k})$ , representing the hopping connectivities in this 4-orbital case is given by

$$\begin{pmatrix} 0 & \varepsilon_{tx} & \varepsilon_{ty} & \varepsilon_{t'} \\ \varepsilon_{tx} & 0 & \varepsilon_{t'} & \varepsilon_{ty} \\ \varepsilon_{ty} & \varepsilon_{t'} & 0 & \varepsilon_{tx} \\ \varepsilon_{t'} & \varepsilon_{ty} & \varepsilon_{tx} & 0 \end{pmatrix}, \quad (3)$$

with  $\varepsilon_{tx} = -2t \cos k_x$ ,  $\varepsilon_{ty} = -2t \cos k_y$  and  $\varepsilon_{t'} = -4t' \cos k_x \cos k_y$ . This matrix is identical in form to that of a  $2 \times 2$  Hubbard cluster with twisted boundary conditions (TBC) [38] where  $\alpha$  is replaced with the site index  $i$  and  $k_x = \theta_x$  and  $k_y = \theta_y$  where  $\theta_x$  and  $\theta_y$  define the TBC.

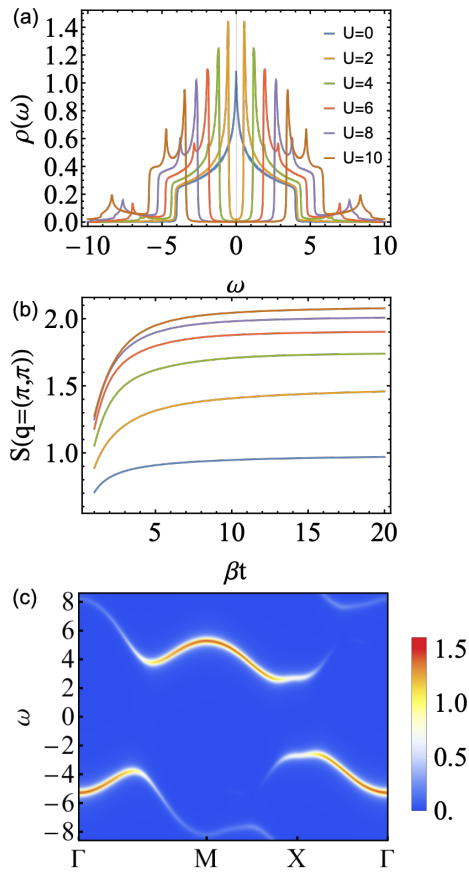


FIG. 4: (a) Density of states representing Mott transition at half-filling of the 4-orbital ( $2 \times 2$ ) HK model at  $\beta = 200/t$ . (b) Spin susceptibility of half-filled OHK model showing a peak at the antiferromagnetic ordering wave vector  $(\pi, \pi)$  and (c) Spectral function  $A(\mathbf{k}, \omega)$  at half-filling with  $U = 8$  and zero temperature with a broadening factor 0.2.

With OHK, however, the twist has a physical interpretation as the crystal momentum, thereby placing OHK in the thermodynamic limit. We compute the density of states for a square lattice ( $t' = 0$ ) and find that any non-zero  $U$  is sufficient to eliminate the metallic state producing a vanishing of the density of states at zero energy as shown in Fig. 4a. Regarding the mechanism of the gap, it cannot be associated with antiferromagnetic order for two reasons. First, AF ordering is prohibited by the Mermin-Wagner theorem[39] at finite temperature in 2d. Also, the charge gap forms at temperatures on the order of  $U$ , well above the AF scale of  $t^2/U$ . Nonetheless, we do find that short-range AF correlations  $S(q = (\pi, \pi)) = \langle \hat{S}^z(q) \hat{S}^z(0) \rangle$  are enhanced by  $U$  which increase and ultimately saturate as  $T$  decreases, all depicted in Fig. 4b. For the half-filled OHK with  $n > 1$ , AF correlations dominate (see supplemental Fig. S8), a qualitative improvement from the band HK model which shows only a diverging ferromagnetic susceptibility. The residual AF correlation in the doped cases (see supplemental Fig. S9) are essential for capturing the underlying intricate physics. The second

reason why the Mott gap cannot be attributed to spin physics is that even in the presence of a nearest-neighbour hopping  $t'$ , the gap vanishes entirely for  $U < U_c$  (see supplemental Fig. S10). However,  $S(\mathbf{q} = (\pi, \pi))$  does not vanish. Consequently, the spin and charge physics are decoupled, an essential feature of Mott physics. Our work here is consistent with the conclusions from quantum cluster methods on the Hubbard model[12]. Also of note is the narrowing of the bands which is completely absent in the band HK model. We then compute the spectral function  $A(\mathbf{k}, \omega)$  at  $U = 8$ , shown in Fig. 4c. The dispersion of the leading excitations are in quantitative agreement with cluster perturbation theory for the 2d square Hubbard model[24, 25] (see supplemental Fig. S11 for the 8-orbital HK result capturing more subtle features). Consequently, OHK with only 4 orbitals already quantitatively describes the known features of the Mott transition.

Given that the kinetic and potential terms do not commute, the number of double occupied sites plays a crucial role in all the ground state properties. To this end, we compute the double occupancy defined as

$$D_n = \frac{1}{N} \sum_{\mathbf{k}, \alpha} \langle n_{\mathbf{k}\alpha\uparrow} n_{\mathbf{k}\alpha\downarrow} \rangle \quad (4)$$

which directly related to the interaction energy. Consider the stark difference between the non-interacting limits of the band and orbital HK models in terms of double occupancy. Regardless of the model, in the non-interacting limit, the expression for  $D_n$  factorizes

$$D_n^{\text{non-int}} = \frac{1}{N} \sum_{\mathbf{k}, \alpha} \langle n_{\mathbf{k}\alpha\uparrow} \rangle \langle n_{\mathbf{k}\alpha\downarrow} \rangle. \quad (5)$$

For the band HK model ( $n = 1$ ), half the BZ is doubly occupied. That is,  $\langle n_{\mathbf{k}\alpha\sigma} \rangle = 1$  if occupied and zero otherwise. Consequently,  $D_1^{\text{non-int}} = 1/2$ . On the other hand, for the orbital model,  $\langle n_{\mathbf{k}\alpha\sigma} \rangle = \langle n_{\mathbf{k}\beta\sigma} \rangle$  for all  $\alpha \neq \beta$  by rotational symmetry. In addition,  $\langle n_{\mathbf{k}\alpha\sigma} \rangle = 1/2$  in the reduced Brillouin zone is not unity as in the band HK model. As a result, we find that for the orbital HK model,  $D_{n>1}^{\text{non-int}} = 1/4$ . Note that this result is identical to the non-interacting limit of the Hubbard model and underscores how drastically band HK differs from its orbital counterpart. Fig. 5a for  $D_n$  shows this dramatic difference. In band HK,  $D$  decreases steadily from  $1/2$  and vanishes for  $U > W$ . However, in orbital HK model,  $D_n$ , starting at  $1/4$ , just tapers asymptotically as  $U$  increases. Note also the rapid convergence between the 2 and 4-orbital cases which matches closely with state-of-the-art auxiliary-field quantum Monte Carlo simulations (AFQMC)[26] and finite-temperature QMC (FTQMC) [23] on the Hubbard model. The inset also shows the double occupancy of the 4-orbital HK model at  $1/8$ -hole-doping ( $x = 0.125$ ) and its benchmark with QMC simulations[26] (see supplement for explanation of the slight mismatch at  $U = 0$  due to definition). The agreement underscores that orbital HK converges rapidly to Hubbard physics. Additionally, the computational cost for solving the 4-orbital HK model is

considerably lower, both in terms of algorithm development (40 lines of Mathematica) and actual code execution, when compared to QMC or cluster-type DMFT simulations on the Hubbard model. Most crucially, the orbital HK model is more amenable to analytical calculations, an aspect we intend to explore deeper in future studies[40].

The fact that the double occupancy only vanishes asymptotically as  $U$  increases in the orbital HK model implies the presence of dynamical mixing between the upper and lower Mott sub-bands. This arises entirely from the non-commutativity[27, 28, 41] of the kinetic and potential energy and appears as  $t/U$  corrections to the low-energy spectral weight (LESW). In the atomic limit, the LESW is strictly  $2x$  (where  $x$  is the doping level) because each hole can be occupied by a spin-up or spin-down electron. Any dynamical corrections to this necessarily generates double occupancy and hence increase the LESW strictly defined as

$$\Lambda(x) \equiv \text{LESW} = \int_0^{\omega_g} N(\omega) d\omega. \quad (6)$$

The  $\omega_g$  locates at the spectral gap in the DOS (see examples in supplemental Fig. S12). In Fig. 5b, we compare the LESW of the 4-orbital HK model with Fig. 3 of Ref. [27]. There is no qualitative difference with ED on the (1d) Hubbard model[27, 28]. Both increase faster than  $2x$ . The semiconductor (dashed line) and Fermi liquid (dashed-dotted) results are shown for comparison. As the occupied part of the lower band has a weight  $1 - x$ , the total weight in the lower band now exceeds  $1 + x$ . As only  $1 + x$  electrons can occupy the lower band, dynamical spectral weight transfer (DSWT) defined as  $\Lambda(x) - 2x$  and plotted in Fig. 5c implies[42] that the spectral weight in the lower band cannot be exhausted by counting electrons alone. Fig. 5c is quantitatively in agreement with the Hubbard model (Fig. 4 of Ref. [27]), the only difference being the maximum value which for 4-orbital HK is 0.2 whereas it is 0.23 for the (1d) Hubbard result. Consequently, that the LESW in the orbital HK model increases faster than  $2x$  is a profoundly non-trivial result as no analytically solvable model has ever been formulated to capture this feature of the Hubbard model.

For any  $n < N_{\text{sites}}$ , the orbital HK model corresponds to a  $N_{\text{sites}}/n$  copies of  $n$ -site Hubbard clusters all connected by TBC. The matrix that determines the TBC is purely local as it is determined by the dynamics. Hence, orbital HK is purely local in the rBZ $_n$  regardless of the number of orbitals used, even  $n = 1$  corresponding to band HK whose locality is illustrated in Fig. 2. *Theorem:* The orbital HK model is equivalent to covering the Brillouin zone with  $N_{\text{sites}}/n$  Hubbard clusters each containing  $n$ -sites all connected via TBC. Clearly, the  $N_{\text{sites}}$ -cluster Hubbard model results when  $n = N_{\text{sites}}$ . Loosely, the  $N_{\text{sites}}/n$  identical copies throughout the Brillouin zone can be thought of as replica copies.

Aside from DSWT, OHK also exhibits a pseudogap in the density of states. Shown in Fig. 6 is the density of states for the 4-orbital HK model with (Fig. 6(a,c)) and without (Fig. 6(b,d)) the next-nearest-neighbor hopping,  $t'$ . Fig. 6(a) shows

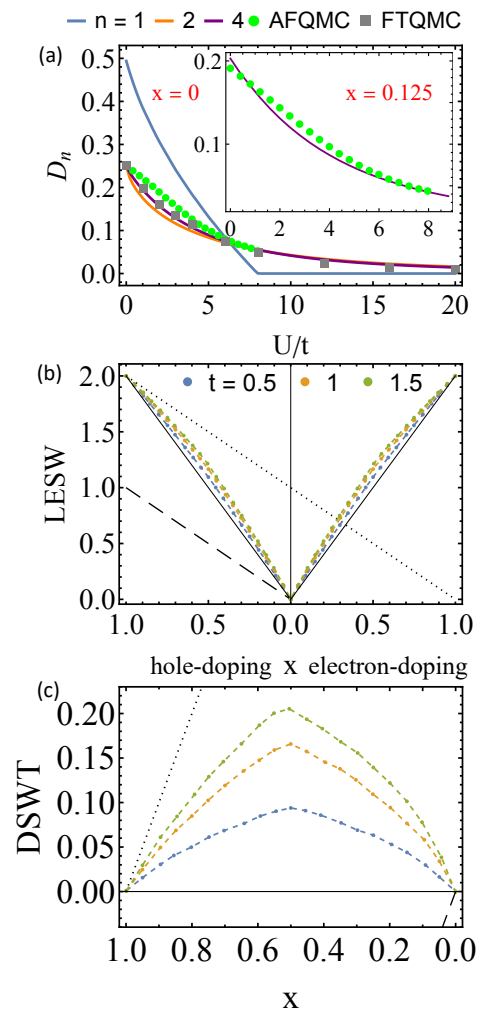


FIG. 5: (a) double occupancy at half-filling ( $x = 0$ ) as a function of  $U$  for the orbital HK model with various  $n$ . The green and gray dots are from auxiliary-field quantum Monte Carlo (AFQMC)[26] and finite-temperature QMC (FTQMC) simulations[23] on the 2D Hubbard model. The inset of panel (a) compares the 4-orbital HK and QMC results[26] at  $1/8$ -hole-doping ( $x = 0.125$ ). LESW and DSWT in the exact solution of the 4-orbital HK model ( $U = 10$ ) for the hopping parameters shown in panels (b) and (c) respectively at  $\beta = 30$ . The solid line shown with slope  $2x$  is the band HK or atomic Hubbard result. The dashed and dotted lines depict the semiconductor and Fermi liquid results respectively. Note, there is no qualitative difference with the ED results for the Hubbard model[27, 28]. As  $t/U$  increases, so does the DSWT.

a suppression of the density of states at the chemical potential ( $\rho(\omega = 0) \lesssim 0.1$ ) in the underdoped region with  $t' = -0.25$  when  $U \geq W$  ( $W = 8t$  is the bare bandwidth), indicative of a pseudogap in the absence of superconducting order. The complete tracking of the density of states at zero frequency in Fig. 6(c) displays the trend that as  $U$  increases, the pseudo-gap region appears and extends to higher hole-doped density. In contrast, when  $t' = 0$ , the pseudo-gap suppression does not arise until  $U \gg W$ , as shown in Fig. 6(b,d). These observa-

tions are consistent with a recent study[38] on a  $2 \times 2$  Hubbard cluster with TBC.

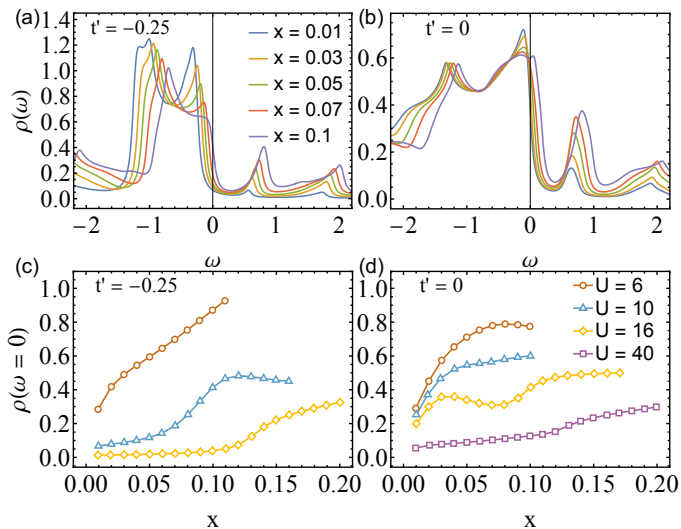


FIG. 6: Density of states at varying hole-doped densities with (a) and without (b) the next-nearest-neighbor hopping  $t'$  for the 4-orbital HK model ( $U/t = 10, \beta = 30/t$ ). Panel (a) and (b) share the same legend. Only for  $t' \neq 0$  is  $\rho(\omega)$  suppressed at zero frequency in the under-doped region, thereby indicating a pseudogap. Panel (c) and (d) show  $\rho(\omega = 0)$  with  $t' = -0.25$  and 0 respectively, as a function of hole-doped density under various  $U$ .

Finally, we compute the heat capacity of the 4-orbital HK model at half-filling shown in Fig. 7. Most noticeable is the two-peak structure at  $U > W$  representing a demarcation of the charge and spin degrees of freedom into high and low-temperature regimes, respectively, consistent with QMC simulations on the Hubbard model [29, 30]. Also at half-filling, we find a near-crossing of the heat capacity curves as a function of  $U$  at a temperature intermediate between the spin and charge excitations. The Maxwell relations governing the entropy dictate[43] such a crossing. Since there is no sign-problem restriction, we can access the low-temperature heat capacity exactly. As we show in Fig. 7(b), the low-temperature heat capacity data follow a power-law increase detailed in the supplement. While such algebraic growth might seem counterintuitive for a Mott insulator, the first-excited state is charge neutral[44, 45] as shown in the supplement. Such charge-neutral excitations determine the low-T behavior of the specific heat and are consistent with the absence of long-range magnetic order.

### SCALING ARGUMENT

The hidden power of the OHK model lies in its convergence properties in higher dimensions. This can be established entirely from the number of degrees of freedom that the orbital number introduces at each  $k$ -point. The quadratic dependence of the Hamiltonian on number operators implies that

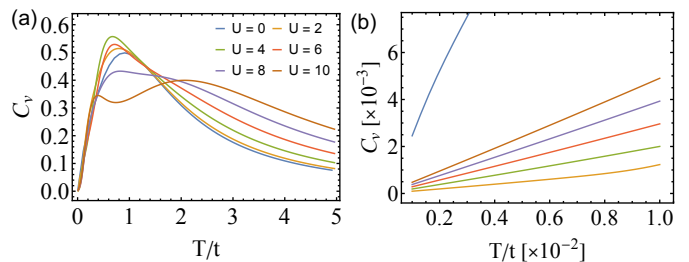


FIG. 7: Heat capacity of the half-filled 4-orbital HK model with various  $U$  at (a) high and (b) low temperatures. Both panels share the same legend.

in 1d, there  $n^2$  pairs of interactions at each  $k$ -point, hence the scaling  $1/n^2$ . In  $d$ -dimensions, the number of degrees is now  $n^{2d}$  for  $n^d$ -orbital HK. Consequently, the convergence to Hubbard, guaranteed by Eq. (2), should scale as  $1/n^{2d}$ . This explains why so few orbitals are needed in 2d relative to 1d to match existing results. In the extreme limit of  $d = \infty$ , we find that this convergence factor vanishes for all  $n > 1$ . Hence,  $n = 1$  or simple band HK is exact in  $d = \infty$ . This further explains why the spectral functions of band HK have a central peak as the Mott insulator is approached (see Fig. (2)) as in DMFT[7]. Note focusing on the operator content is valid only if a fixed point exists. We have shown that HK represents a fixed point[31, 37] as it contains the most relevant interaction with scaling dimension  $-2$  thereby breaking the  $Z_2$  symmetry[31, 37] at the Fermi surface of a Fermi liquid. Adding orbitals to each  $k$ -point does not lead to further momentum integrations as such decorations (new degrees of freedom) of each  $k$ -point just appear as discrete summations. Hence, the convergence to the fixed point should just be determined by the total number of degrees freedom at each  $k$ -point, namely  $n^{2d}$ . Consequently, the fixed point[31, 37] controls Mott physics.

### CONCLUDING REMARKS:

The connection between OHK to Hubbard physics can also be understood in terms of momentum scattering. In the band HK model, the interaction is local in  $k$  space and only zero momentum scattering/transfer obtains, while in the Hubbard model, the scattering momenta include all  $q$  in the BZ. As we add orbitals to the band HK model, we effectively add additional momentum scattering. For example, the 2-orbital HK includes  $q = (\pi, \pi)$ , and 4-orbital HK includes  $q = (\pi, \pi), (0, \pi), (\pi, 0)$ . A rigorous derivation to show this can be found in the supplement. That few-orbital HK already captures quantitatively Hubbard physics supports the flow to Hubbard through a hierarchy of momentum scattering.

The rapid convergence to Hubbard points to a new hybrid approach for OHK in higher dimensions: use DMRG for one of the directions and OHK on the others. Because of the rapid convergence of OHK, such an approach would essentially be

exact. Consequently, OHK opens up a fundamentally new approach for simulations on strongly correlated electron matter as a result of the fixed point[37]. Moreover, given the consistent evolution of physical quantities with increasing orbital number, it is more amenable to machine learning techniques than are other methods. This consistent evolution allows machine learning algorithms to detect patterns and make predictions more effectively, which could facilitate the discovery of new phases and transitions in these systems by leveraging the power of data-driven approaches.

**Acknowledgements** We thank Barry Bradlyn for helpful comments and Shiwei Zhang for sending us his double occupancy data that is plotted in Fig. 5a (green dots) and George Sawatzky for a helpful e-mail exchange. This work was supported by the Center for Quantum Sensing and Quantum Materials, a DOE Energy Frontier Research Center, grant DE-SC0021238 (P. M. and P. W. P.). PWP also acknowledges NSF DMR-2111379 for partial funding of the HK work which led to these results.

- 
- [1] B.-X. Zheng, C.-M. Chung, P. Corboz, G. Ehlers, M.-P. Qin, R. M. Noack, H. Shi, S. R. White, S. Zhang, and G. K.-L. Chan, *Science* **358**, 1155 (2017).
- [2] E. W. Huang, C. B. Mendl, H.-C. Jiang, B. Moritz, and T. P. Devereaux, *npj Quantum Materials* **3**, 22 (2018).
- [3] M. Qin, C.-M. Chung, H. Shi, E. Vitali, C. Hubig, U. Schollwöck, S. R. White, and S. Zhang (Simons Collaboration on the Many-Electron Problem), *Phys. Rev. X* **10**, 031016 (2020), URL <https://link.aps.org/doi/10.1103/PhysRevX.10.031016>.
- [4] M. Qin, H. Shi, and S. Zhang, *Phys. Rev. B* **94**, 085103 (2016), URL <https://link.aps.org/doi/10.1103/PhysRevB.94.085103>.
- [5] J. P. F. LeBlanc, A. E. Antipov, F. Becca, I. W. Bulik, G. K.-L. Chan, C.-M. Chung, Y. Deng, M. Ferrero, T. M. Henderson, C. A. Jiménez-Hoyos, et al. (Simons Collaboration on the Many-Electron Problem), *Phys. Rev. X* **5**, 041041 (2015), URL <https://link.aps.org/doi/10.1103/PhysRevX.5.041041>.
- [6] H.-C. Jiang and S. A. Kivelson, *Proceedings of the National Academy of Sciences* **119**, e2109406119 (2022).
- [7] A. Georges, G. Kotliar, W. Krauth, and M. J. Rozenberg, *Reviews of Modern Physics* **68**, 13 (1996).
- [8] W. Xu, K. Haule, and G. Kotliar, *Phys. Rev. Lett.* **111**, 036401 (2013), URL <https://link.aps.org/doi/10.1103/PhysRevLett.111.036401>.
- [9] X. Deng, J. Mravlje, R. Žitko, M. Ferrero, G. Kotliar, and A. Georges, *Phys. Rev. Lett.* **110**, 086401 (2013), URL <https://link.aps.org/doi/10.1103/PhysRevLett.110.086401>.
- [10] H. Park, K. Haule, and G. Kotliar, *Phys. Rev. Lett.* **101**, 186403 (2008), URL <https://link.aps.org/doi/10.1103/PhysRevLett.101.186403>.
- [11] S. S. Kancharla, B. Kyung, D. Sénéchal, M. Civelli, M. Capone, G. Kotliar, and A.-M. S. Tremblay, *Phys. Rev. B* **77**, 184516 (2008), URL <https://link.aps.org/doi/10.1103/PhysRevB.77.184516>.
- [12] T. Maier, M. Jarrell, T. Pruschke, and M. H. Hettler, *Rev. Mod. Phys.* **77**, 1027 (2005), URL <https://link.aps.org/doi/10.1103/RevModPhys.77.1027>.
- [13] P. Mai, S. Karakuzu, G. Balduzzi, S. Johnston, and T. A. Maier, *Proceedings of the National Academy of Sciences* **119**, e2112806119 (2022).
- [14] P. Mai, N. S. Nichols, S. Karakuzu, F. Bao, A. Del Maestro, T. A. Maier, and S. Johnston, *Nature Communications* **14**, 2889 (2023).
- [15] P. Werner, E. Gull, O. Parcollet, and A. J. Millis, *Phys. Rev. B* **80**, 045120 (2009), URL <https://link.aps.org/doi/10.1103/PhysRevB.80.045120>.
- [16] T. D. Stanescu and G. Kotliar, *Phys. Rev. B* **74**, 125110 (2006), URL <https://link.aps.org/doi/10.1103/PhysRevB.74.125110>.
- [17] M. Ferrero, P. S. Cornaglia, L. De Leo, O. Parcollet, G. Kotliar, and A. Georges, *Phys. Rev. B* **80**, 064501 (2009), URL <https://link.aps.org/doi/10.1103/PhysRevB.80.064501>.
- [18] W. Wu, M. S. Scheurer, S. Chatterjee, S. Sachdev, A. Georges, and M. Ferrero, *Phys. Rev. X* **8**, 021048 (2018), URL <https://link.aps.org/doi/10.1103/PhysRevX.8.021048>.
- [19] E. Gull, A. J. Millis, and O. Parcollet, p. 1 (2012), URL [http://inis.iaea.org/search/search.aspx?orig\\_q=RN:48038267](http://inis.iaea.org/search/search.aspx?orig_q=RN:48038267).
- [20] E. W. Huang, R. Sheppard, B. Moritz, and T. P. Devereaux, *Science* **366**, 987 (2019).
- [21] P. T. Brown, D. Mitra, E. Guardado-Sanchez, R. Nourafkan, A. Reymbaut, C.-D. Hébert, S. Bergeron, A.-M. S. Tremblay, J. Kokalj, D. A. Huse, et al., *Science* **363**, 379 (2019).
- [22] Y. Hatsugai and M. Kohmoto, *Journal of the Physical Society of Japan* **61**, 2056 (1992), <https://doi.org/10.1143/JPSJ.61.2056>, URL <https://doi.org/10.1143/JPSJ.61.2056>.
- [23] S. R. White, D. J. Scalapino, R. L. Sugar, E. Y. Loh, J. E. Gubernatis, and R. T. Scalettar, *Phys. Rev. B* **40**, 506 (1989), URL <https://link.aps.org/doi/10.1103/PhysRevB.40.506>.
- [24] K. Seki and S. Yunoki, *Phys. Rev. B* **93**, 245115 (2016), URL <https://link.aps.org/doi/10.1103/PhysRevB.93.245115>.
- [25] E. W. Huang, S. Ding, J. Liu, and Y. Wang, *Phys. Rev. Res.* **4**, L042015 (2022), URL <https://link.aps.org/doi/10.1103/PhysRevResearch.4.L042015>.
- [26] H. Xu, H. Shi, E. Vitali, M. Qin, and S. Zhang (2024), unpublished.
- [27] M. B. J. Meinders, H. Eskes, and G. A. Sawatzky, *Phys. Rev. B* **48**, 3916 (1993).
- [28] H. Eskes, M. B. J. Meinders, and G. A. Sawatzky, *Phys. Rev. Lett.* **67**, 1035 (1991), URL <https://link.aps.org/doi/10.1103/PhysRevLett.67.1035>.
- [29] D. Duffy and A. Moreo, *Phys. Rev. B* **55**, 12918 (1997), URL <https://link.aps.org/doi/10.1103/PhysRevB.55.12918>.
- [30] W. O. Wang, J. K. Ding, B. Moritz, E. W. Huang, and T. P. Devereaux, *Phys. Rev. B* **105**, L161103 (2022), URL <https://link.aps.org/doi/10.1103/PhysRevB.105.L161103>.
- [31] E. W. Huang, G. L. Nave, and P. W. Phillips, *Nature Physics* **18**, 511 (2022), URL <https://doi.org/10.1038%2Fs41567-022-01529-8>.
- [32] A. S. Wightman, *Phys. Rev.* **101**, 860 (1956), URL <https://link.aps.org/doi/10.1103/PhysRev.101.860>.
- [33] D. Manning-Coe and B. Bradlyn, *Phys. Rev. B* **108**, 165136 (2023), URL <https://link.aps.org/doi/10.1103/>

- PhysRevB.108.165136.
- [34] P. Mai, B. E. Feldman, and P. W. Phillips, Phys. Rev. Res. **5**, 013162 (2023), URL <https://link.aps.org/doi/10.1103/PhysRevResearch.5.013162>.
  - [35] P. Mai, J. Zhao, B. E. Feldman, and P. W. Phillips, Nature Communications **14**, 5999 (2023), URL <https://doi.org/10.1038/s41467-023-41465-6>.
  - [36] C. Setty, S. Sur, L. Chen, F. Xie, H. Hu, S. Paschen, J. Cano, and Q. Si, arXiv e-prints arXiv:2301.13870 (2023), 2301.13870.
  - [37] J. Zhao, G. La Nave, and P. W. Phillips, Phys. Rev. B **108**, 165135 (2023), URL <https://link.aps.org/doi/10.1103/PhysRevB.108.165135>.
  - [38] E. W. Huang, arXiv e-prints arXiv:2010.12601 (2020), 2010.12601.
  - [39] N. D. Mermin and H. Wagner, Phys. Rev. Lett. **17**, 1133 (1966), URL <https://link.aps.org/doi/10.1103/PhysRevLett.17.1133>.
  - [40] G. Tenkila, J. Zhao, and P. W. Phillips, arXiv e-prints arXiv:2406.17846 (2024), 2406.17846.
  - [41] A. B. Harris and R. V. Lange, Phys. Rev. **157**, 295 (1967), URL <https://link.aps.org/doi/10.1103/PhysRev.157.295>.
  - [42] P. Phillips, Rev. Mod. Phys. **82**, 1719 (2010), URL <https://link.aps.org/doi/10.1103/RevModPhys.82.1719>.
  - [43] D. Vollhardt, Phys. Rev. Lett. **78**, 1307 (1997), URL <https://link.aps.org/doi/10.1103/PhysRevLett.78.1307>.
  - [44] P. Mai, J. Zhao, T. A. Maier, B. Bradlyn, and P. W. Phillips, *Topological phase transition without single-particle-gap closing in strongly correlated systems* (2024), 2401.01402.
  - [45] J. Zhao, P. Mai, B. Bradlyn, and P. Phillips, Phys. Rev. Lett. **131**, 106601 (2023), URL <https://link.aps.org/doi/10.1103/PhysRevLett.131.106601>.

# New Approach to Strong Correlation: Twisting Hubbard into the Orbital Hatsugai-Kohmoto Model: supplemental material

Peizhi Mai<sup>1</sup>, Jinchao Zhao<sup>1</sup>, Gaurav Tenkila<sup>1</sup>, Nico A. Hackner<sup>1</sup>, Dhruv Kush<sup>1</sup>, Derek Pan<sup>1</sup>, Philip W. Phillips<sup>1,†</sup>  
<sup>1</sup>Department of Physics and Institute of Condensed Matter Theory,  
 University of Illinois at Urbana-Champaign, Urbana, IL 61801, USA

## ONE-DIMENSIONAL BENCHMARK

In this section, we present the OHK results in one dimension (1d) and make comparison with exact diagonalization (ED) and density matrix renormalization group (DMRG). In Fig. S1a, we show the difference between ground state energy in OHK with different orbital number  $n$  and the exact Bethe ansatz result for 1d Hubbard. With  $n \geq 10$ , the energy difference is less than 1%. Further, the difference decreases consistently with increasing  $n$  for all  $U$ . Fig. S1b shows that ED of a Hubbard  $n$ -site cluster results in random finite-size effects especially for small  $U$ . Fig. S1c, we show the standard DMRG calculation for 1d Hubbard chain with different lengths and open boundary condition (OBC). As is evident, OHK and DMRG (for large enough system sizes) are in agreement.

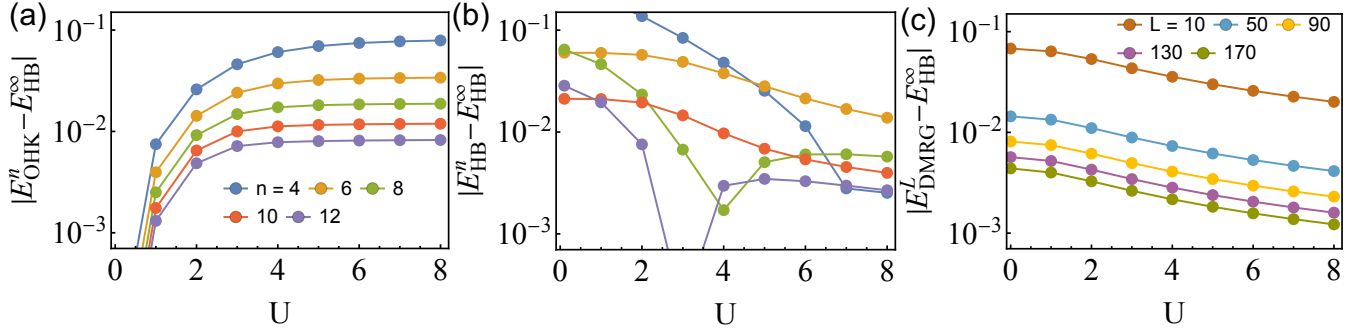


FIG. S1: Comparison of the deviation in ground-state energy relative to the infinite Hubbard chain's ground-state energy from the Bethe ansatz ( $E_{\text{HB}}^{\infty}$ ). (a) Deviation for the  $n$ -orbital HK model ( $E_{\text{OHK}}^n$ ); (b) Deviation for the periodic  $n$ -site Hubbard chain solved with ED ( $E_{\text{HB}}^n$ ). Panels (a) and (b) share the same legend. (c) Deviation for the DMRG simulation on a Hubbard chain with length  $L$  ( $E_{\text{DMRG}}^L$ ).

As we mention in the discussion section of the main text, orbital-HK provides a series of alternative models that can be solved using state-of-the-art numerical methods, apart from ED. Here we present the example of using DMRG to solve the orbital-HK model in 1-d in Fig. S3. In this way, we can easily include 20 orbitals and complete the computation in a personal computer. The combination of OHK and DMRG improves from the standard DMRG for the Hubbard model with length  $L = 170$  in the sense that it also depicts the small-to-intermediate  $U$  results accurately. Again, the OHK results converge to the asymptotic exact result rapidly and consistently (no fluctuation or sign change). This significantly facilitates data-driven techniques like machine learning to predict the uncomputed region like the large  $n$  limit. To demonstrate this, we choose the data from Fig. S3 at  $U = 4, 6, 8$  respectively and conduct the polynomial regression fitting for each case. The results are shown in Fig. S3. Thanks to the consistent behavior of the OHK data, the extrapolation to  $n \rightarrow \infty$  limit results in a much smaller error at least one order smaller than the 40-orbital simulation for each  $U$ . The asymptotic values for  $n \rightarrow \infty$  are  $-5.4 \times 10^{-5}$  ( $U = 4$ ),  $-9 \times 10^{-5}$  ( $U = 6$ ),  $-4 \times 10^{-5}$  ( $U = 8$ ). We find great match using the simple function  $f(1/n) = a * (1/n)^\gamma$  to estimate the fitting, where  $c$  is the estimated asymptotic value at  $n \rightarrow \infty$  mentioned above and  $\gamma$  is the power determining the speed of convergence. For each case,  $f(U = 4) = 0.45(1/n^{1.83})$ ,  $f(U = 6) = 0.51(1/n^{2.01})$  and  $f(U = 8) = 0.45(1/n^{2.07})$ . The error bars for  $a$  and  $\gamma$  are on the order of  $10^{-3}$ . For comparison, we also show the ground state energy error from standard DMRG simulation on a Hubbard chain in Fig. S3(b) for  $U = 4$ . That gives a linear scaling as the inverse length ( $1/L$ ). Comparing Fig. S3(a) and (b), we can see the combining OHK and DMRG improves the convergence speed considerably from the standard DMRG.

In Fig. S4, we show the single-particle charge gap as a function of  $U$  from solving orbital HK and conducting DMRG simulations, in comparison with the exact Bethe ansatz result. Bethe ansatz gives an essential singularity in the thermodynamic limit. Orbital HK captures the vanishing gap at  $U = 0$  and slowly converges to the exponential singularity at small  $U$  as orbital number increases. For large  $U = 10$ , the deviation is less than 1% just with  $n = 12$  orbitals. On the other hand, DMRG captures

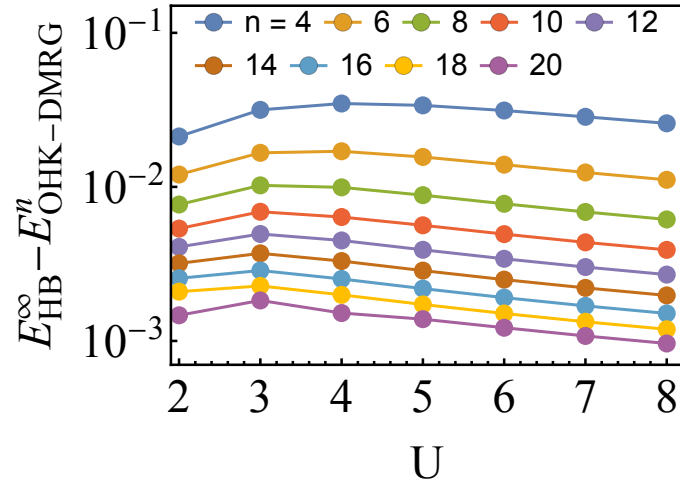


FIG. S2: Comparison of the error in ground-state energy for Orbital-HK model solved by DMRG relative to the infinite Hubbard chain's ground-state energy from the Bethe ansatz ( $E_{\text{HB}}^{\infty}$ )

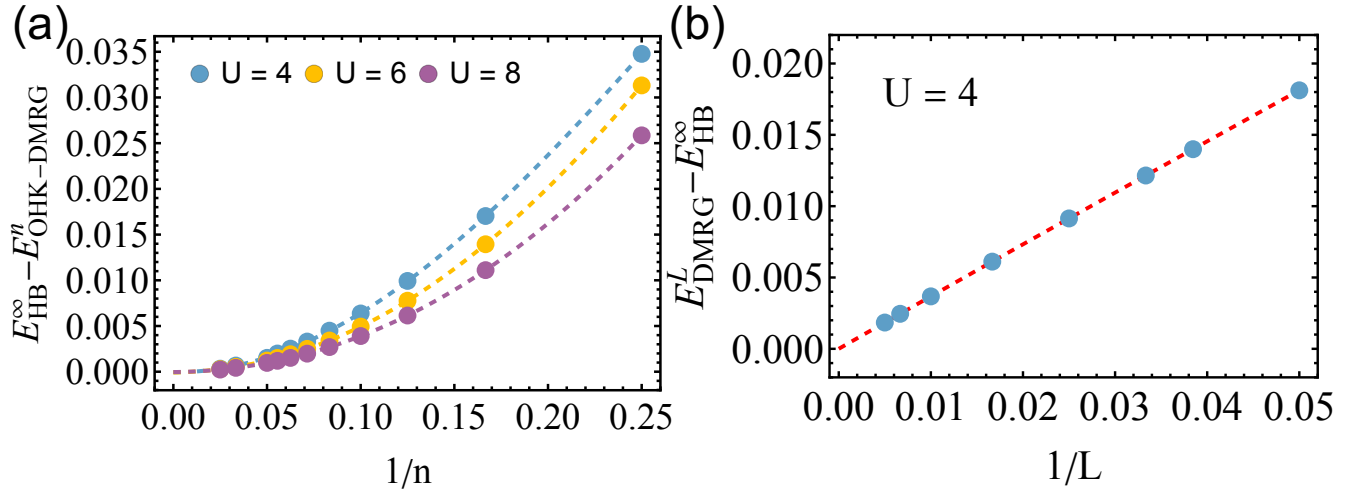


FIG. S3: (a) The error of ground state energy from orbital-HK model solved with DMRG at  $U = 4, 6, 8$  and the corresponding fitting by machine learning polynomial regression. The fitting extrapolates to the limit  $1/n = 0 (n \rightarrow \infty)$ . The asymptotic values at  $1/n = 0$  are  $-5.4 \times 10^{-5}$  ( $U = 4$ ),  $-9 \times 10^{-5}$  ( $U = 6$ ),  $-4 \times 10^{-5}$  ( $U = 8$ ). (b) The ground state energy from standard DMRG on a Hubbard chain is given at  $U = 4$ .

the larger  $U$  accurately but slowly converges to the correct  $U = 0$  limit due to finite length. This provides further evidence that OHK is in the thermodynamic limit. It is the averaging over the crystal momentum that distinguishes it from ED.

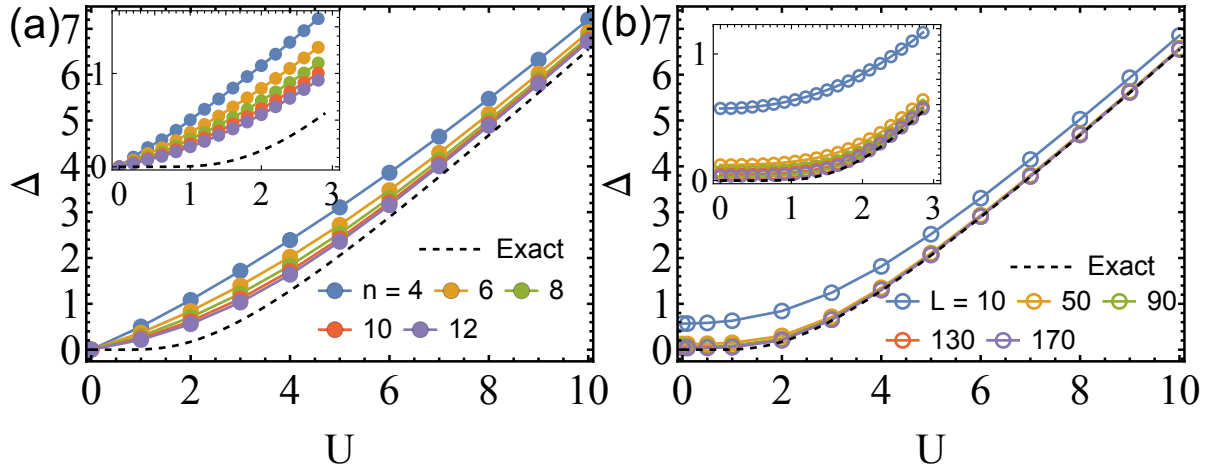


FIG. S4: The single-particle charge gap obtained from (a) solving the  $n$ -orbital HK model ( $E_{\text{OHK}}^n$ ); (b) solving a Hubbard chain with length  $L$  using DMRG. In both panels, the dashed line represents the exact result from Bethe ansatz. The insets provide a zoom-in view of the small  $U$  region. In OHK the gap vanishes at  $U = 0$ , whereas in DMRG it is finite as a result of the finite size of the system.

## TWO DIMENSIONS

## Single-particle correlation in band HK

In this section, we provide further details of the hole correlation function for the band HK model. First, we show the hole correlation function at  $\langle n \rangle = 0.5, 0.75, 1$  with  $U = 10$  in comparison with the non-interacting case at corresponding  $2\langle n \rangle$  in Fig. S5, all at the same temperature  $\beta = 50$ . For each case,  $g_h(\langle n \rangle, U = 10)$  overlaps completely with the  $g_h(2\langle n \rangle, U = 0)/2$ , indicating the singly occupied nature of the lower Mott band and the commutativity between the kinetic and potential energy terms in band HK. In Fig. S5c, the correlation decay sharply rendering it completely local. Regarding the other two cases  $\langle n \rangle = 0.5, 0.75$ , Fig. S6 shows that they decay following a power law. As there is no difference in the fall-off in the non-interacting and HK models, the measure of locality is identical for both.

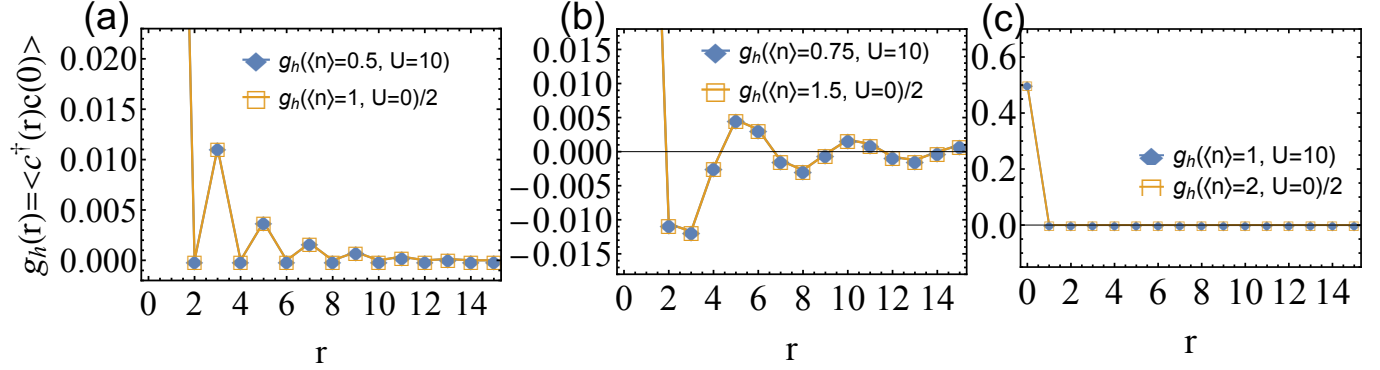


FIG. S5: The comparison in hole Green function (for one spin) between band HK model at density  $\langle n \rangle$  with  $U = 10, \beta = 50$  and the non-interacting tight-binding model at density  $2\langle n \rangle$  with the same temperature. (a)  $\langle n \rangle = 0.5$ ; (b)  $\langle n \rangle = 0.75$ ; (c)  $\langle n \rangle = 1$ .

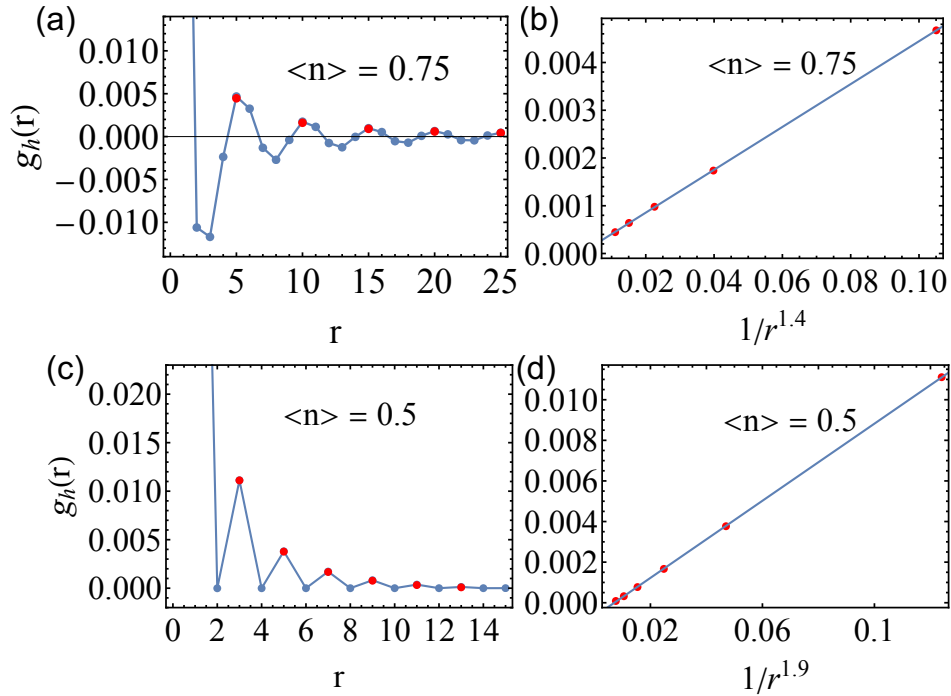


FIG. S6: The fitting of hole Green function from band HK model at  $U = 10, \beta = 50$  to algebraic behavior. The first row is for  $\langle n \rangle = 0.75$ , and the second row for  $\langle n \rangle = 0.5$ . The left and right panels in each row share the same red dots.

### Reduced Brillouin Zone

Here we depict (see Fig. S7) an alternative construction to decreasing the size of the BZ simply by grouping sites together to form larger unit cells. In this sense, OHK has some consilience with Wilson/Kadanoff renormalization[? ]. Thus far, we have been unable to establish this rigorously as the OHK scheme is reversible, that is no projection to the reduced cell.

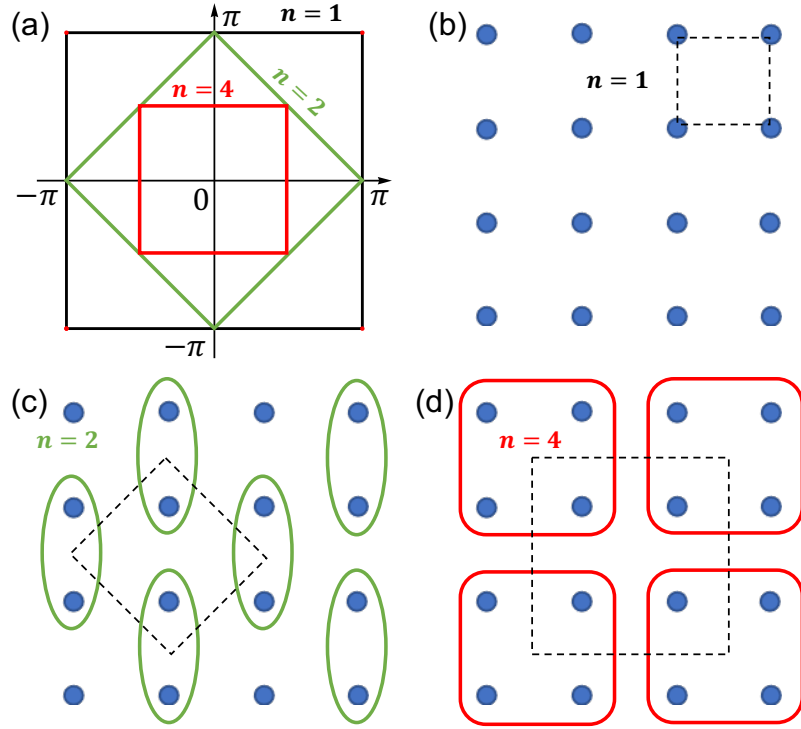


FIG. S7: (a) Evolution of the reduced Brillouin zone (with the constraint  $N \times n = N_{\text{sites}}$ ) as the number of orbitals ( $n$ ) increases, leading to a purely local (in  $\mathbf{k}$ -space) model when  $n = N_{\text{sites}}$ . Alternative real-space construction by grouping the atoms into cells (encircled by green/red lines) with an updated lattice constant. (b) Original unit cell in the band HK model with primitive unit cell in dashed line. (c) The 2-atom (orbital) HK model leads to a doubling of the unit cell size and the lattice constant (dashed line) (d) The 4-orbital HK model results in a quadrupling of the unit cell size. When  $n = N_{\text{sites}}$ , the unit cell contains all the sites.

### Mott transition and spin correlation

In this section, we provide more details for the Mott transition and the corresponding spin correlation. We show the spin correlation at  $U = 10$  at three scattering momenta for the 4-orbital HK model in Fig. S8(a). The  $q = (\pi, \pi)$  case dominates the spin correlation, indicating the leading magnetic fluctuation is of the antiferromagnetic (AF) type. In Fig. S8(b), we show the AF correlation for different orbital-HK. As the number of orbitals increases from 1 (band HK), the AF correlation strengthens, and thus it gives a qualitatively better simulation of Hubbard physics. We then look into the density away from half-filling. In Fig. S9, we see that the AF correlation remains for a wide range of doping, which is essential for simulating the complicated doping physics in the Hubbard model.

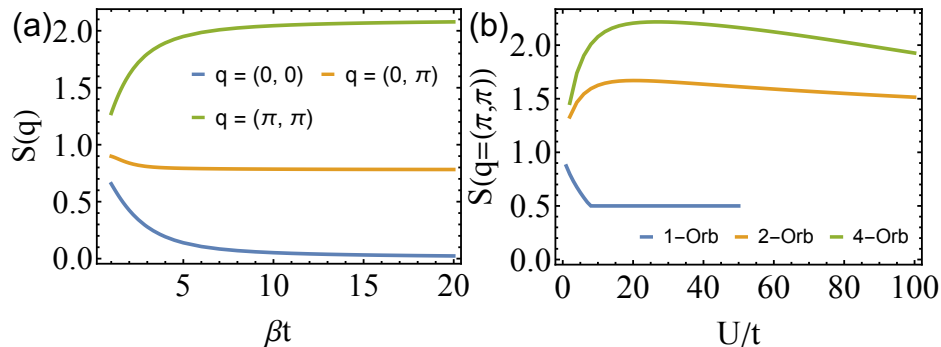


FIG. S8: (a) Equal-time spin correlation for different transfer momenta  $q$  at  $U = 10$  for 4-orbital HK. (b) Equal-time antiferromagnetic correlation as a function of  $U$  for different orbital-HK model

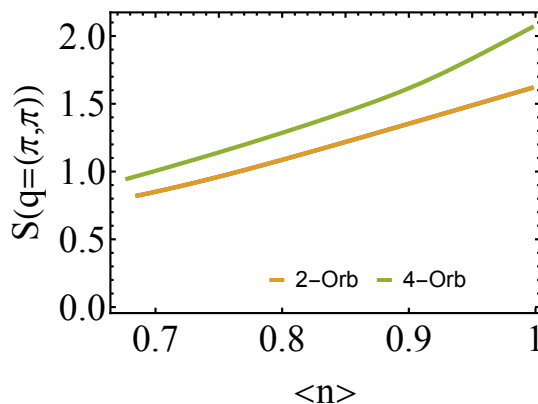


FIG. S9: Equal-time antiferromagnetic correlation as a function of density at  $U = 10, \beta t = 20$  for 2- and 4-orbital HK models.

In the main text, we show that for 4-orbital HK with  $t' = 0$ , the gap at half-filling opens at any finite  $U$ , namely the non-existence of a Mott transition. This is the special case with perfect Fermi surface nesting in the non-interacting limit. We now turn on  $t' = -0.25$ . Fig. S10(a) shows that the system remains gapless for small  $U$  and opens a gap starting from a critical  $U$ , indicating a Mott transition. We further explore the AF correlation at  $U = 0.5$  for  $t' = 0$  and  $-0.25$  in Fig. S10(a), corresponding to gapped and gapless respectively in the weak coupling limit. Since the AF correlations, Fig. S10(b) do not vanish once  $t'$  is turned on but the gap vanishes (for  $U < U_c$ ), there is no connection between AF correlations and the Mott gap. Fig. S10(c) shows the  $U_c$  as a function  $|t'|$  (the sign of  $t'$  does not make a difference in  $U_c$ ). Initially,  $U_c$  grows almost linearly with  $|t'|$ . It saturates around  $|t'| \approx 0.55$  and then decreases with further increasing  $|t'|$ .

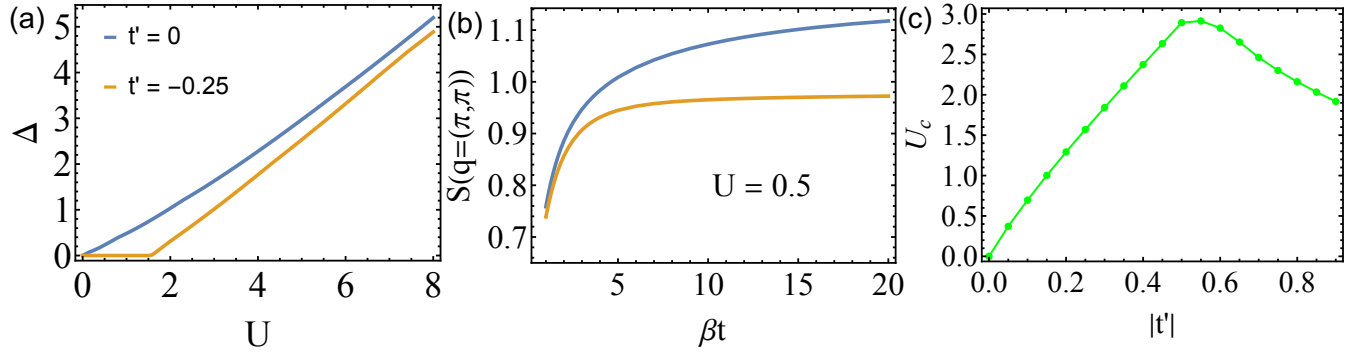


FIG. S10: (a) Evolution of single-particle charge gap with  $U$  at half-filling for  $t' = 0$  and  $t' = -0.25$ . (b) Equal-time antiferromagnetic correlation at  $U = 0.5$  for  $t' = 0$  and  $t' = -0.25$  (same legend as panel (a)). (c) The critical interaction strength  $U_c$  for Mott transition as a function  $|t'|$ .

### Spectral function at half-filling

In this section, we show the half-filled spectral function at  $U = 8$  for the 4- (Fig. S11(a)) and 8-orbital (Fig. S11(c)) HK model, in comparison with several methods, particularly cluster perturbation theory (CPT) on the Hubbard model. We can see that already for the 4-orbital case, the essential leading features such as peak positions and gap estimates are qualitatively close to CPT. Note that 4-orbital HK allows an analytical insight. The 8-orbital HK result improves adding details to the much weaker sub-leading feature closely. This underscores that as  $n \rightarrow N_{\text{sites}}$ , OHK becomes the Hubbard model.

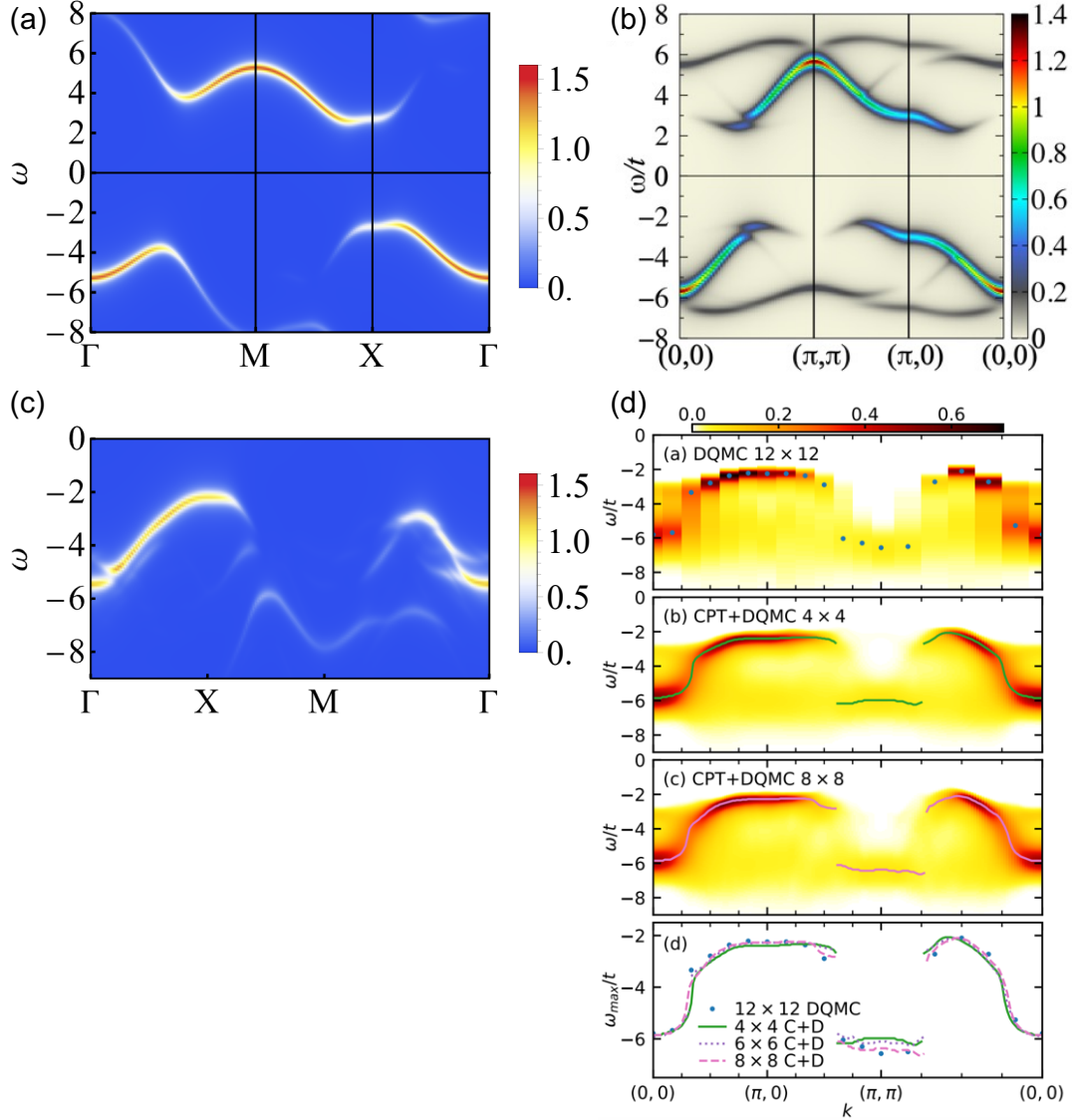


FIG. S11: Comparison in the half-filled ( $U = 8$ ) spectral function  $A(\mathbf{k}, \omega)$  between orbital-HK models (at zero  $T$  with a Lorentzian broadening of 0.2) and other methods for solving Hubbard model. (a) 4-orbital HK; (b)  $2 \times 2$  Cluster perturbation theory (the panel is taken from Phys. Rev. B 93.245115); (c) 8-orbital ( $2 \times 4$ ) HK; (d) several methods (the panel is taken from Phys. Rev. Research 4, L042015) at  $\beta = 16$ .

### Low energy spectral weight

In this section, we explain that the integral for low energy spectral weight defined in the Eq. (6) depends on the cut-off  $\omega_g$ .  $\omega_g$  is chosen at the gap in density of states at a fixed density. We demonstrate this point with some examples in Fig. S12 for different densities.

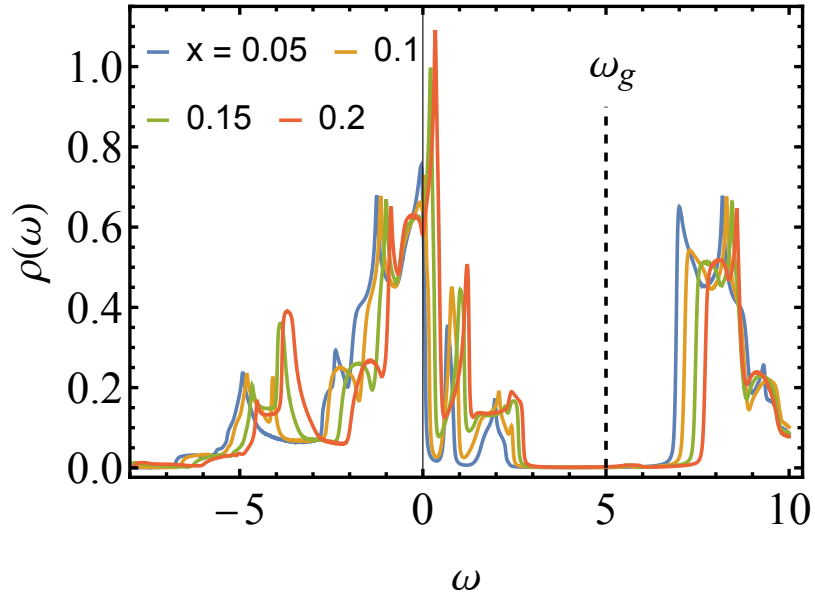


FIG. S12: Density of states for the 4-orbital HK model at varying hole-doped densities  $x$  with  $U = 10, \beta = 30$ . The cutoff  $\omega_g$  is chosen at the gap for calculating the low energy spectral weight with Eq. (6).

### Heat capacity

A drastic difference between the single band HK and a multi-orbital HK model is the energy gap between the ground state and the first excited state. Unlike the band HK model, the gap for OHK closes at a surface of points in the Brillouin zone where  $\varepsilon(k)$  vanishes. Here  $\varepsilon(k)$  is the lowest eigenvalue of the non-interacting Hamiltonian. Since the ground state and the first excited state have the same occupation numbers, the excitation is charge neutral and thus the system remains an insulator. Around this surface, the gap is proportional to

$$E_k^1 - E_k^0 = \frac{1}{2} \left( -U + \sqrt{U^2 + 16\varepsilon(k)^2} \right) \approx \frac{4\varepsilon(k)^2}{U} \dots \quad (\text{S1})$$

This behavior is universal in both  $N_\alpha = 2, 4$  orbital HK models. From now on we focus on the  $N_\alpha = 2$  case. The first excitation energy has a degeneracy  $d > 1$ . If we set  $\mu = U/2$ , we may ignore all the other excited states that are at least  $U/2$  above them. In the low -temperature regime  $\beta U/2 \gg 1$ , the total energy simplifies to

$$\begin{aligned} E(T) &\approx \sum_k \left( \frac{de^{-\beta E_k^1}}{Z} E_k^1 + \frac{e^{-\beta E_k^0}}{Z} E_k^0 \right) \\ &= \sum_k E_k^0 + \sum_k \frac{de^{-\beta E_k^1}}{Z} (E_k^1 - E_k^0) \\ &\approx E(0) + \sum_k \left( \frac{de^{-\beta \frac{4\varepsilon(k)^2}{U}}}{de^{-\beta \frac{4\varepsilon(k)^2}{U}} + 1} \frac{4\varepsilon(k)^2}{U} \right) \\ &= E(0) + \int d\varepsilon D(\varepsilon) \frac{d}{d + e^{\frac{4\beta\varepsilon^2}{U}}} \frac{4\varepsilon^2}{U}, \end{aligned} \quad (\text{S2})$$

where  $D(\varepsilon)$  is the density of states in terms of the lowest eigenvalue  $\varepsilon$  of the non-interacting Hamiltonian. At low temperature  $\beta t^2 \gg U$ , the integrand decays quickly as a function of  $\varepsilon$ . Thus if  $D(\varepsilon)$  does not vanish or have any singularity at  $\varepsilon = 0$ , we have

$$\begin{aligned} E(T) &\approx E(0) + D(0) \frac{\sqrt{U}}{2} \int dx \frac{dx^2}{d + e^{\beta x^2}} \\ &= E(0) - D(0) \frac{\sqrt{U}}{2} \frac{\sqrt{\pi}}{2} \text{Li}_{3/2}(-d) (k_B T)^{3/2}, \end{aligned} \quad (\text{S3})$$

where  $\text{Li}_n(z)$  is the polylogarithmic function and  $\text{Li}_{3/2}(-d) < 0$  when  $d > 0$ . Thus, the heat capacity becomes

$$C_v = -\frac{3\sqrt{\pi}}{8} \text{Li}_{3/2}(-d) D(0) k_B \sqrt{U k_B T}. \quad (\text{S4})$$

For the case when  $D(\varepsilon) \propto \varepsilon^\lambda$ , we have

$$\begin{aligned} E(T) - E(0) &\propto \int dx \frac{x^{2+\lambda}}{d + e^{\beta x^2}} \\ &\propto -\Gamma \left( \frac{3+\lambda}{2} \right) \text{Li}_{(3+\lambda)/2}(-d) (k_B T)^{(3+\lambda)/2}. \end{aligned} \quad (\text{S5})$$

By taking the temperature derivative, we obtain a  $T^{(1+\lambda)/2}$  dependence for  $C_v$ . This power law dependence on  $T$  surfaces from the charge-neutral excitation gap in the Mott insulating state, which is absent in band HK or trivial insulators which have an inverse exponential  $\exp(-\Delta/T)$  dependence instead. This behavior can be observed in the heat capacity of the  $N_\alpha = 1, 2, 4$  orbital HK model in Fig. S13.

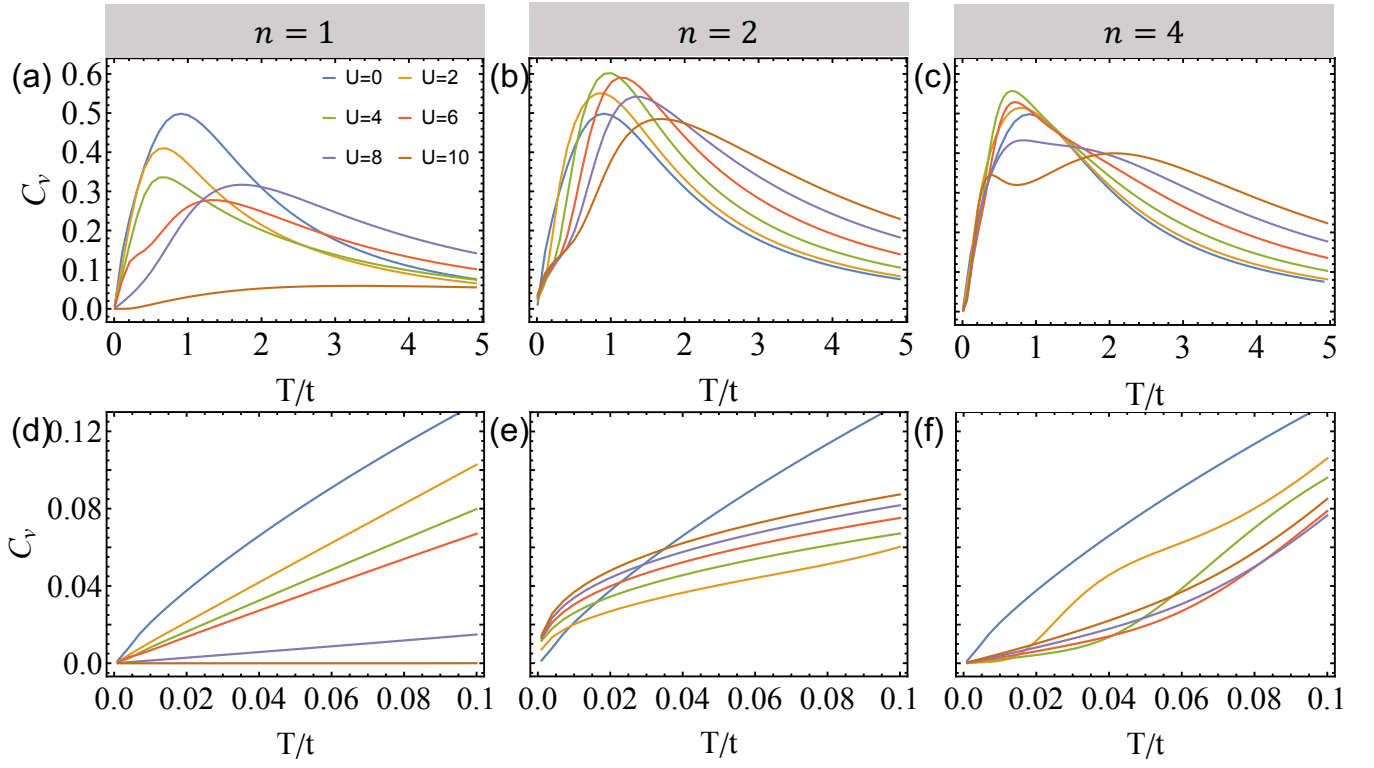


FIG. S13: Heat capacity for orbital-HK models with different number of orbitals  $N_\alpha = 1, 2, 4$  as labelled. Panels (a-c) are for high temperature, while panels (d-f) are for low temperatures.

### Momentum space operators for OHK

We list the relation between the momentum space Fermion operators in the original and orbital bases. The original momentum space Fermion operators are expressed in terms of real space operators,

$$c_{\mathbf{k}\sigma} = \frac{1}{\sqrt{N_{\text{sites}}}} \sum_{\mathbf{r}} e^{-i\mathbf{k}\cdot\mathbf{r}} c_{\mathbf{r}\sigma}, \quad (\text{S6})$$

where  $N$  is the total number of sites and the summation over  $\mathbf{r}$  is on the full lattice. Thus the momentum  $\mathbf{k}$  takes its value from the original Brillouin zone.

The Fermion operators in the orbital basis, which was intensively used in this paper, are defined upon regrouping  $n$  sites into a unit cell and re-labeling them  $\alpha = 1, \dots, n$ . The  $n$ -orbital momentum space Fermion operators are defined as:

$$c_{\mathbf{k}\alpha\sigma}^{(n)} = \frac{1}{\sqrt{N_{\text{sites}}/n}} \sum_{\mathbf{R}} e^{-i\mathbf{k}\cdot(\mathbf{R}+\mathbf{r}_\alpha)} c_{\mathbf{R}+\mathbf{r}_\alpha\sigma}, \quad (\text{S7})$$

where  $\mathbf{r}_\alpha$  is the crystal basis and the summation over  $\mathbf{R}$  is on the new lattice of the expanded unit cell. Thus the momentum  $\mathbf{k}$  takes value from the reduced Brillouin zone. From this, we can derive a relationship between  $c_{\mathbf{k}\alpha\sigma}$  and  $c_{\mathbf{k}\sigma}$ :

$$\begin{aligned} c_{\mathbf{k}\alpha\sigma}^{(n)} &= \frac{\sqrt{n}}{N_{\text{sites}}} \sum_{\mathbf{R}} \sum_{\mathbf{k}' \in \text{BZ}} e^{-i(\mathbf{k}-\mathbf{k}')\cdot(\mathbf{R}+\mathbf{r}_\alpha)} c_{\mathbf{k}'\sigma} \\ &= \frac{\sqrt{n}}{N_{\text{sites}}} \sum_{\mathbf{k}' \in \text{BZ}} \delta_{(n)}(\mathbf{k}-\mathbf{k}') e^{-i(\mathbf{k}-\mathbf{k}')\cdot\mathbf{r}_\alpha} c_{\mathbf{k}'\sigma} \\ &= \frac{1}{\sqrt{n}} \sum_{\mathbf{b}_i \text{ in FBZ}} e^{-i\mathbf{b}_i\cdot\mathbf{r}_\alpha} c_{\mathbf{k}+\mathbf{b}_i\sigma}, \end{aligned} \quad (\text{S8})$$

where  $\mathbf{b}_i$  are the reciprocal lattice vectors of the expanded lattice and they shall lie in the first original Brillouin zone(FBZ). For example, for the 2-orbital unit cell as defined in Fig. S7(c), the momentum space operators satisfy

$$\begin{aligned} c_{\mathbf{k}1\sigma}^{(2)} &= \frac{1}{\sqrt{2}}(c_{\mathbf{k}\sigma} + c_{\mathbf{k}+(\pi,\pi)\sigma}), \\ c_{\mathbf{k}2\sigma}^{(2)} &= \frac{1}{\sqrt{2}}(c_{\mathbf{k}\sigma} - c_{\mathbf{k}+(\pi,\pi)\sigma}). \end{aligned} \quad (\text{S9})$$

For the 4-orbital unit cell as defined in Fig. S7(d), the momentum space operators satisfy

$$\begin{aligned} c_{\mathbf{k}1\sigma}^{(4)} &= \frac{1}{2}(c_{\mathbf{k}\sigma} + c_{\mathbf{k}+(\pi,0)\sigma} + c_{\mathbf{k}+(0,\pi)\sigma} + c_{\mathbf{k}+(\pi,\pi)\sigma}) \\ c_{\mathbf{k}2\sigma}^{(4)} &= \frac{1}{2}(c_{\mathbf{k}\sigma} - c_{\mathbf{k}+(\pi,0)\sigma} + c_{\mathbf{k}+(0,\pi)\sigma} - c_{\mathbf{k}+(\pi,\pi)\sigma}) \\ c_{\mathbf{k}3\sigma}^{(4)} &= \frac{1}{2}(c_{\mathbf{k}\sigma} + c_{\mathbf{k}+(\pi,0)\sigma} - c_{\mathbf{k}+(0,\pi)\sigma} - c_{\mathbf{k}+(\pi,\pi)\sigma}) \\ c_{\mathbf{k}4\sigma}^{(4)} &= \frac{1}{2}(c_{\mathbf{k}\sigma} - c_{\mathbf{k}+(\pi,0)\sigma} - c_{\mathbf{k}+(0,\pi)\sigma} + c_{\mathbf{k}+(\pi,\pi)\sigma}). \end{aligned} \quad (\text{S10})$$

Thus, the orbital-HK interaction term  $n_{\mathbf{k}A\uparrow}n_{\mathbf{k}A\downarrow} + n_{\mathbf{k}B\uparrow}n_{\mathbf{k}B\downarrow}$  would contain scatterings among  $\mathbf{k}$  and  $\mathbf{k} + \mathbf{b}_i$ , which is the scattering in the original Brillouin zone vectors but now defined in terms of the reciprocal lattice vectors of the expanded lattice.

### Double Occupancy

Let's consider the double occupancy of the  $n$ -orbital HK model as defined in Eq.(4) in the non-interacting limit,

$$\begin{aligned} D_n &= \frac{1}{N_{\text{sites}}} \sum_{\mathbf{k} \in \text{rBZ}_n} \sum_{\alpha=1}^n \langle n_{\mathbf{k}\alpha\uparrow} n_{\mathbf{k}\alpha\downarrow} \rangle \\ &= \frac{1}{N_{\text{sites}}} \sum_{\mathbf{k} \in \text{rBZ}_n} \sum_{\alpha=1}^n \langle n_{\mathbf{k}\alpha\uparrow} \rangle \langle n_{\mathbf{k}\alpha\downarrow} \rangle. \end{aligned} \quad (\text{S11})$$

According to Eq.(S8), the average value of the number operator is

$$\begin{aligned}
\langle n_{\mathbf{k}\alpha\sigma} \rangle &= \langle c_{\mathbf{k}\alpha\sigma}^{(n)\dagger} c_{\mathbf{k}\alpha\sigma}^{(n)} \rangle \\
&= \frac{1}{n} \sum_{\mathbf{b}_i \text{ in FBZ}} \sum_{\mathbf{b}_j \text{ in FBZ}} e^{i(\mathbf{b}_j - \mathbf{b}_i) \cdot \mathbf{r}_\alpha} \langle c_{\mathbf{k} + \mathbf{b}_i\sigma}^\dagger c_{\mathbf{k} + \mathbf{b}_j\sigma} \rangle \\
&= \frac{1}{n} \sum_{\mathbf{b}_i \text{ in FBZ}} \langle n_{\mathbf{k} + \mathbf{b}_i\sigma} \rangle,
\end{aligned} \tag{S12}$$

where in the last step we have dropped all the terms that do not conserve the momentum and notice that this result does not depend on  $\alpha$ . The double occupancy is thus

$$\begin{aligned}
D_n &= \frac{1}{N_{\text{sites}}} \sum_{\mathbf{k} \in \text{rBZ}_n} \sum_{\alpha=1}^n \langle n_{\mathbf{k}\alpha\uparrow} \rangle \langle n_{\mathbf{k}\alpha\downarrow} \rangle \\
&= \frac{1}{N_{\text{sites}} n} \sum_{\mathbf{k} \in \text{rBZ}_n} \left( \sum_{\mathbf{b}_i \text{ in FBZ}} \langle n_{\mathbf{k} + \mathbf{b}_i\sigma} \rangle \right)^2.
\end{aligned} \tag{S13}$$

As was explained in the main text, at half filling  $D_1$  differs from all the other  $D_n$  for  $n > 1$ . For the doped system, all the  $D_n$ s are different. As an example, for the doping level  $x = 1/8$ , the Hubbard limit gives  $n = N$  and  $D_N = (7/16)^2 \approx 0.1914$ , while in the 4-orbital case, the result is different.  $x = 1/8$  hole doping will result in  $1/4$  part of the reduced Brillouin zone having occupancy  $\sum_{\alpha\sigma} n_{\mathbf{k}\alpha\sigma} = 2$ , while the remaining  $3/4$  part of the reduced Brillouin zone having occupancy  $\sum_{\alpha\sigma} n_{\mathbf{k}\alpha\sigma} = 4$ , the overall filling factor is thus  $(\frac{1}{4} \times 2 + \frac{3}{4} \times 4) / 8 = \frac{7}{16}$ . The double occupancy thus reads,

$$\begin{aligned}
D_4 &= \frac{1}{N_{\text{sites}}} \sum_{\mathbf{k} \in \text{rBZ}_n} \sum_{\alpha=1}^n \langle n_{\mathbf{k}\alpha\uparrow} \rangle \langle n_{\mathbf{k}\alpha\downarrow} \rangle \\
&= \frac{1}{4} (2/8)^2 + \frac{3}{4} (4/8)^2 \\
&= 0.203 \neq D_{N_{\text{sites}}}.
\end{aligned} \tag{S14}$$